Icarus 215 (2011) 62–74

Contents lists available at ScienceDirect

Icarus

journal homepage: www.elsevier.com/locate/icarus

Saturn's zonal wind profile in 2004–2009 from Cassini ISS images and its long-term variability

E. García-Melendo [a,b,*], S. Pérez-Hoyos [c], A. Sánchez-Lavega [c], R. Hueso [c]

[a] Fundació Privada Observatori Esteve Duran, 08553 Seva, Spain
[b] Institut de Ciències de l'Espai (CSIC-IEEC), Campus UAB, Facultat de Ciències, Torre C5, parell, 2a pl., E-08193 Bellaterra, Spain
[c] Departamento de Física Aplicada I, Escuela Superior de Ingeniería, Universidad del País Vasco, Alameda Urquijo s/n, 48013 Bilbao, Spain

ARTICLE INFO

Article history:
Received 9 February 2011
Revised 2 July 2011
Accepted 5 July 2011
Available online 19 July 2011

Keywords:
Saturn, Atmosphere
Atmospheres, Dynamics

ABSTRACT

Five years of Cassini Imaging Science Subsystem images, from 2004 to 2009, are analyzed in this work to retrieve global zonal wind profiles of Saturn's northern and southern hemispheres in the methane absorbing bands at 890 and 727 nm and in their respective adjacent continuum wavelengths of 939 and 752 nm. A complete view of Saturn's global circulation, including the equator, at two pressure levels, in the tropopause (60 mbar to 250 mbar with the MT filters) and in the upper troposphere (from ~350 mbar to ~500 mbar with the CB filter set), is presented. Both zonal wind profiles (available at the Supplementary Material Section), show the same structure but with significant differences in the peak of the eastward jets and the equatorial region, including a region of positive vertical shear symmetrically located around the equator between the $10° < |\varphi_c| < 25°$ where zonal velocities close to the tropopause are higher than at 500 mbar. A comparison of previously published zonal wind sets obtained by Voyager 1 and 2 (1980–1981), Hubble Space Telescope, and ground-based telescopes (1990–2004) with the present Cassini profiles (2004–2009) covering a full Saturn year shows that the shape of the zonal wind profile and intensity of the jets has remained almost unchanged except at the equator, despite the seasonal insolation cycle and the variability of Saturn's emitted power. The major wind changes occurred at equatorial latitudes, perhaps following the Great White Spot eruption in 1990. It is not evident from our study if the seasonal insolation cycle and its associated ring shadowing influence the equatorial circulation at cloud level.

1. Introduction

The giant planets have atmospheric circulations dominated by latitude-alternating East–West jets. Our knowledge and understanding of the physical causes governing these patterns is still poor (Ingersoll et al., 2004; Del Genio et al., 2009), although it is improving thanks to laboratory experiments and theoretical work (e.g. Read et al., 2007; Jones and Kuzanyan, 2009; Kaspi et al., 2009). Saturn's rotation axis, in contrast to that of Jupiter, is tilted by 26.7°, therefore its atmosphere undergoes a strong 30-year-long seasonal cycle where the subsolar point oscillates within a 50° band around the equator. Saturn also has a ring system whose shadow almost completely blocks the solar radiation directed to the winter hemisphere probably influencing the seasonal cycle (e.g. Pérez-Hoyos and Sánchez-Lavega, 2006a). In addition, with an apparent seasonal regularity, planetary scale convective storms called Great White Spots (GWS), develop at the equator and other latitudes injecting important amounts of aerosols and compounds from deeper levels, changing the cloud structure, and consequently the radiative balance (Acarreta and Sánchez Lavega, 1999; Pérez-Hoyos and Sánchez-Lavega, 2006a), and modifying the atmospheric circulation in the stratosphere (Sayanagi and Showman, 2007; Fletcher et al., 2011) although less apparently at the upper cloud and deeper levels (Sánchez-Lavega et al., 1991, 2011; Hueso and Sánchez-Lavega, 2004).

Due to the higher value of the atmospheric scale height in Saturn's upper troposphere (~25 km in Jupiter and ~45 km in Saturn), hazes and cloud layers extend vertically much higher than in Jupiter, up to the tropopause (see for example West et al., 2009). Observing the atmosphere of the planet at different wavelengths with filters sensing cloud reflectivity at different altitudes, such as the continuum and methane absorbing bands, allows us to probe the winds at pressure levels separated by hundreds of mbar, and to study their dynamics and relationship with the temperature field through the thermal wind, assuming jets are in geostrophic balance at the cloud tops, at least outside the equatorial region. It is expected that even if the origin of Saturn's zonal winds is rooted within the deep convective movements, and therefore

* Corresponding author at: Fundació Privada Observatori Esteve Duran, 08553 Seva, Spain.
E-mail address: egarcia@foed.org (E. García-Melendo).

0019-1035/$ - see front matter © 2011 Elsevier Inc. All rights reserved.
doi:10.1016/j.icarus.2011.07.005

presumably stable in time as proposed by different calculations (Heimpel and Aurnou, 2007), the seasonal insolation cycle should affect the dynamics of the measurable winds at the upper troposphere due to the relatively low values of the radiative constant (Conrath and Pirraglia, 1983). While the Hubble Space Telescope (HST) has allowed to monitor Jupiter winds between space missions (see for example Simon-Miller, 1999; García-Melendo and Sánchez-Lavega, 2001), high resolution observations of Saturn are more difficult. Cloud tracers show a small angular size from Earth and display a very low contrast due to the presence of a permanent haze in the upper troposphere with an optical thickness higher than unity (Tomasko et al., 1984; Karkoschka and Tomasko, 1992, 2005; Ortiz et al., 1996; Muñoz et al., 2004; Pérez-Hoyos et al., 2005; see a review in Pérez-Hoyos and Sánchez-Lavega (2006b)). As a consequence, retrieving the zonal wind profile has only been possible from spacecraft observations, and partially in some occasions using HST images. For these reasons, the only detailed measurements of Saturn's winds before the Cassini Mission were obtained from Voyager observations in 1980 and 1981 (Smith et al., 1982; Ingersoll et al., 1984; Sánchez-Lavega et al., 2000), and yet they were incomplete due to the partial blocking of Saturn's equator by the rings.

A detailed knowledge of Saturn's zonal wind profile in time is an essential piece of information to make progress in understanding its origin and dynamics. Indeed, Voyager and Cassini zonal wind profiles show differences at the equator difficult to reconcile (García-Melendo et al., 2010), and it is clear that these differences will not be fully understood until we have observations of saturnian winds and other important physical variables through a complete seasonal cycle and particularly during the rare convective GWS events (Sánchez_Lavega, 1982; Sánchez-Lavega et al., 1991, 1996).

In this paper we present measurements of the mean zonal winds in Saturn obtained from Cassini ISS images during the 2004–2009 period and compare the wind profiles with measurements from HST and the Voyagers. In Section 2 we describe our set of observations, the methods used to retrieve the winds and the errors of wind retrievals. In Section 3 we present the Cassini high resolution average wind results for the respective CB and MT filter sets including tabulated data at each latitude. In Section 4 we compare these new profiles with existing historical Voyager and HST observations. In Section 5 we discuss the general wind results. We summarize our conclusions in Section 6.

2. Observations and data reduction

2.1. Dataset

Data presented in this study were derived from images acquired by the Cassini Imaging Science Subsystem (ISS) instrument (Porco et al., 2004) onboard the Cassini spacecraft from late 2004, 3 months after its orbital insertion around Saturn in June 30, to early 2009. The first frames used for our wind measurements were collected almost 2 years after Saturn's northern hemisphere winter solstice, when the subsolar point was at the planetocentric latitude of ~24°S. In the last early 2009 images the subsolar point was at ~3.5°S, when the planet was close to its northern spring equinox. We analyzed ~300 frames taken by the Wide and Narrow Angle ISS Cameras with image resolution ranging between 160 km pix^{-1} and 30 km pix^{-1}. Our analysis includes images mostly obtained in the intermediate (MT2, 727 nm), and strong (MT3, 890 nm) methane absorption band filters, and in their respective adjacent continuum filters CB2 (752 nm), and CB3 (939 nm). Comparatively, the Cassini spacecraft took few images with the MT1 and CB1 (619 nm) filters mounted in the Narrow Angle Camera and only a few MT1 frames were useful for our purposes. Table 1 is the observation log for the selected Cassini data.

2.2. Image navigation

We used the Planetary Laboratory Image Analysis (PLIA) software to navigate Cassini images (Hueso et al., 2010). PLIA automatically fits an ellipse on the projected image of the planet on the image plane according to the navigation information provided by the Spacecraft Planet Instrument C-matrix Event (SPICE) kernels stored in PDS labels of the image (Acton, 1995). To make sure that comparison between image navigation and the limb position is accurate, PLIA software also allows human supervision to correct limb fitting. Saturn navigation was performed adopting the respective equatorial and polar radii at the 1 bar level of 60,268 km and 54,364 km (Seidelmann et al., 2007). Images with only a small portion of visible limb were avoided due to the difficulties in checking image navigation accuracy.

2.3. Zonal winds measurements

Zonal velocities were measured by performing automatic one dimensional cross-correlation of brightness longitude scans as described in García-Melendo and Sánchez-Lavega (2001). This procedure is based on the assumption that small cloud tracers preserve their physical integrity during the time span of one planet rotation. Longitude brightness scans then map the distribution of cloud tracers at a given latitude, which are advected by the zonal flow. To measure zonal velocities, we selected pairs of ISS images separated by approximately one Saturn rotation (~10.6 h). Each image was navigated to build a cylindrical projection with a spatial resolution of 0.1° in both longitude and latitude from which we retrieved the longitudinal brightness scans at each latitude. Pairs of scans extracted at the same latitude were automatically compared by performing a one dimensional cross-correlation. The position of the correlation maximum gave the longitudinal displacement between both scans and it therefore served to compute the zonal velocity given the time elapsed between the two frames. Longitude scan pairs

Table 1
Observation log of the Cassini images used to retrieve Saturn zonal winds.

COISS volume	Filters	Date interval (yyyy/mm/dd)	Number of images	Resolution (km pix^{-1})	Subsolar point latitude
2006	CB2, MT1, MT2	2004/09/06–2004/09/13	64	60	−23.9
2009	CB2, MT3	2005/02/25–2005/02/27	51	160	−22.5
2010	CB2, MT3	2005/02/27	15	160	−22.5
2012	CB2, MT2	2005/06/15–2005/06/16	54	140	−21.4
2026	CB2, MT2	2006/10/11	9	30	−15.4
2042	CB2, MT2, CB3, MT3	2008/02/25–2008/02/27	40	90	−8.1
2043	CB2, MT3	2008/03/29	24	80	−7.7
2046	CB2, MT2, CB3, MT3	2008/06/19–2008/06/20	24	70	−6.4
2050	CB2	2008/11/29–2008/12/01	7	40	−3.9
2051	CB2, MT2, CB3, MT3	2008/12/28	16	60	−3.5
2052	MT2, MT3	2009/01/01–2009/01/12	8	60	−3.5

usually covered from the planet's limb to the terminator, and its length depended on the visible illuminated portion of the planet, which in turn is a function of illumination conditions (sub-solar point latitude) and the planet-spacecraft geometry (sub-spacecraft latitude and phase angle). For example, when the spacecraft is over a high latitude, extracted brightness scans close to the pole can cover a much longer longitude interval than those near the equator if the sub-solar point is also at a high latitude. Brightness scans typically spanned between 50 and 100 longitude degrees. We did not construct cylindrical projections by merging several images to avoid different drift values for tracers located at different longitudes due to time differences between consecutive image pairs. Since correlation results are dominated by albedo transitions between adjacent tracers, we enhanced them by applying unsharp mask and Butterworth filters (e.g., Hueso et al., 2010) to the original and projected images. Individual one-dimensional scans were also high-pass filtered and normalized to remove possible limb-darkening effects, and brightness and contrast differences between scans. Sánchez-Lavega et al. (2000) describe how zonal velocities are computed once longitudinal displacements are extracted for a tracer, which we also apply here.

There is uncertainty on the actual Saturn's rotation period for a valid reference frame in which winds must be measured (see, for instance, Sánchez-Lavega, 2005; Showman, 2009). Following preceding authors and to be consistent with their measurements (e. g. Smith et al., 1982; Ingersoll et al., 1984; Godfrey, 1988; Barnet et al., 1992; Sánchez-Lavega et al., 2000, 2006, 2007; Porco et al., 2004; Vasavada et al., 2006; Del Genio et al., 2007; Dyudina et al., 2008; García-Melendo et al., 2009; Baines et al., 2009; Choi et al., 2009), we adopt the Saturn kilometric radiation (SKR) period measured by the Voyager mission (Desch and Kaiser, 1981) used to define System III rotating frame where $\Omega_{III} = 810.7939024$ deg day^{-1} (Seidelmann et al., 2007). Although this longitude system is adequate for relative comparison with previous datasets, it might not be precise for absolute zonal wind measurements. See Read et al. (2009) for a re-definition of the rotation rate of Saturn and a discussion on its implications.

2.4. Measurement errors

For automatic one-dimensional cross-correlation wind retrieval, the main error sources are navigation uncertainties, intrinsic variability of the cloud tracers (Sánchez-Lavega et al., 2000), local dynamics effects such as waves, vortices, divergent movements (García-Melendo and Sánchez-Lavega, 2001), and scarcity of tracers at some domains of the planet such as the regions close to the mid latitude jet peaks. All of them may alter the position of the cross-correlation maximum peaks. For images with the worst spatial resolution (160 km pix^{-1} at the subspacecraft's point) a one pixel navigation error translates into a formal $\sim$4 m s^{-1} uncertainty. As measurements are performed away from the subspacecraft point P_S, positional errors increase as sec(α), where α is the angle between the subspacecraft point P_S and the normal of the measured surface element, which means a $\sim$12 m s^{-1} error when α reaches 70°. Such an extreme case is not significant: it is at least an order of magnitude smaller than the intensity of the jet peaks and, given the large number of image pairs, brightness scans are not fetched that far from P_S. As we will see, average values of the standard deviation are well below this limit.

In total, more than 60,000 wind measurements were extracted from $\sim$150 image pairs. All data points for the same family of wavelengths (to be discussed later), were merged in a single profile and divided in small latitude bins. Individual velocity measurements within a given bin were averaged to obtain a mean profile. Inside every bin at the planetocentric latitude φ_c, we used the sample mean $\langle u_\lambda(\varphi_c)\rangle$ for wavelength λ

$$\langle u_\lambda(\varphi_c)\rangle = \frac{\sum_{i=1}^{N_\lambda(\varphi_c)} u_\lambda(\varphi_c)_i}{N_\lambda(\varphi_c)} \quad (1)$$

(from now on we will use planetocentric latitudes and represent it by φ_c), $N_\lambda(\varphi_c)$ is the number of points in the current bin and wavelength λ, and $u_\lambda(\varphi_c)_i$ are the individual zonal speed measurements obtained from different image pairs in the filter with effective wavelength λ. The error $\delta u_\lambda(\varphi_c)$ for every average point was estimated by using the unbiased sample standard deviation

$$\delta u_\lambda(\varphi_c) = \left\{ \frac{\sum_{i=1}^{N_\lambda(\varphi_c)} (u_\lambda(\varphi_c)_i - \langle u_\lambda(\varphi_c)\rangle)^2}{N_\lambda(\varphi_c) - 1} \right\}^{1/2}. \quad (2)$$

Taking into account that we wish to distinguish clouds at different pressure levels moving at different zonal speeds, a comment on the simultaneous measurement of tracers moving at different velocities is also timely. Automatic 1D correlation is very efficient in detecting a large number of albedo transitions corresponding to the same cloud tracers moving at the same speed. If we had tracers moving at different speeds they would add noise to the correlation results (position of cross-correlation maxima), and the retrieved wind profiles would not be repetitive. The obtained repetitive low scatter velocity profiles for the MT and CB filters, especially where zonal velocity measurements are different, tells us that we are actually looking at different cloud tracers at the two different pressure levels probed by the two filter sets. This is also clear when examining the different cloud structures at those layers as discussed by Sánchez-Lavega et al. (2007) and García-Melendo et al. (2010). This remark raises the question of whether we are looking at the same tracers where the CB and MT velocity profiles are coincident. We will show later that the answer is no. At those latitudes there is almost no vertical shear but our retrieval methods track different clouds.

3. Wind results

We obtained two distinct zonal wind patterns, one for the continuum CB family filters, and another one for the methane absorbing band MT filters. In total, over 35,000 wind measurements were collected in CB2 and CB3 covering planetocentric latitudes from 90°S to 85°N, and over 26,000 in MT2 and MT3, spanning a latitude range from 80°S to 73°N. Our obtained data are fully consistent with the partial profiles from Cassini data reported by other authors (Porco et al., 2004; Vasavada et al., 2006; Sánchez-Lavega et al., 2006, 2007; García-Melendo et al., 2009, 2010) but extend those results towards northern latitudes and allow to study the wind profiles in time over the observation period.

3.1. The zonal wind profile between 2004 and 2009

During the September 2004 to January 2009 period, the southern hemisphere was continuously visible, while the northern hemisphere was not accessible until the rings shadow receded to the equator in 2008. With data at the two cloud layers spanning a 6 years period in the southern hemisphere we can check if short-term wind variability occurs during the southern hemisphere summer. At the deeper levels sensed by the CB filters, from $\sim$350 mbar to $\sim$700 mbar (though this range may be deeper see, Pérez-Hoyos and Sánchez-Lavega (2006b), Sánchez-Lavega et al. (2007), and García-Melendo et al. (2009, 2010)) we expect, in principle, little or no variability during this period produced by the seasonal insolation cycle due to the high value of the radiative time constant τ_R, $\sim$1 Saturn year for 350 mbar and $\sim$2.5 Saturn years for 700 mbar according to Conrath and Pirraglia (1983). Fig. 1 shows the superposition of nine individual CB2 and CB3 profiles at different periods and at different latitude ranges measured

between 2004 and 2008. We cannot distinguish any important variation, even between 2004 and 2008 in the southern hemisphere and the equator. In the northern hemisphere, winds were measured during a shorter time interval spanning less than a year during 2008 and no changes were detected. However, MT2 and MT3 filters show clouds and hazes at higher altitudes at pressures between 60 mbar (equatorial region) and 250 mbar at other higher latitudes (see references above) At these pressure levels the radiative time constant is much smaller, between 0.3 and 0.6 saturnian years (Conrath and Pirraglia, 1983; Barnet, 1990), and we could reasonably expect wind variations, although we detected none. Fig. 2 shows the seven individual average MT2 and MT3 profiles retrieved between September 2004 and January 2009. As in the CB2 and CB3 case, we do not see any changes larger than data uncertainty. This is true even when comparing the first wind profiles in 2004 to the last 2009 profiles in the southern hemisphere. A slight difference amounting to no more than 20 m s^{-1} at 11°S and 16°S between September 2004 and December 2008, suggests a change in the shape of the profile in that region of the southern equatorial profile, but the magnitude of this apparent change is uncertain and uncorroborated by our cloud tracking measurements of the equatorial region between 2004 and 2008 (García-Melendo et al., 2010) which do not reveal any changes within the ~20 m s^{-1} data scatter.

The stability of the wind profiles in the two CB and MT family filters justifies computing the average high resolution CB and MT profiles which cover almost the whole planet. We followed similar procedures as those presented in García-Melendo and

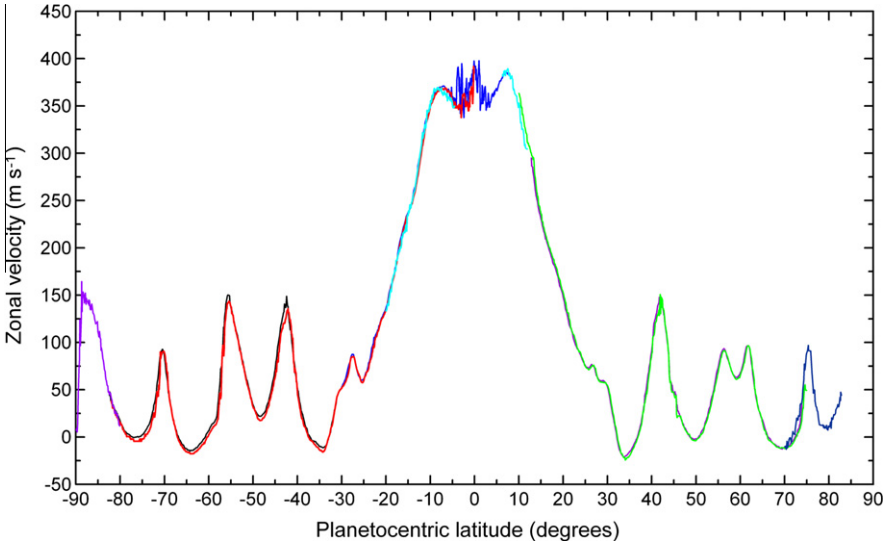

Fig. 1. Individual zonal wind profiles measured between September 2004 and December 2008 from Cassini ISS CB2 and CB3 images. Nine profiles are superimposed for the time periods listed in Table 1 where: (black) COISS 2006 covering the latitude interval from 82°S to 30°S; (blue) COISS 2009 from 30°S to 8°N; (red) COISS 2012 from 83°S to 0°; (blue purple) COISS 2026 from 90°S to 80°S; (purple) COISS 2042 from 12°N to 74°N; (green) COISS 2046 from 10°N to 75°N; (navy blue) COISS 2050 from 70°N to 83°N; (cyan) COISS 2051 from 20°S to 5°S; (cyan) COISS 2051 from 6°N to 12°N. (For interpretation of the references to color in this figure legend, the reader is referred to the web version of this article.)

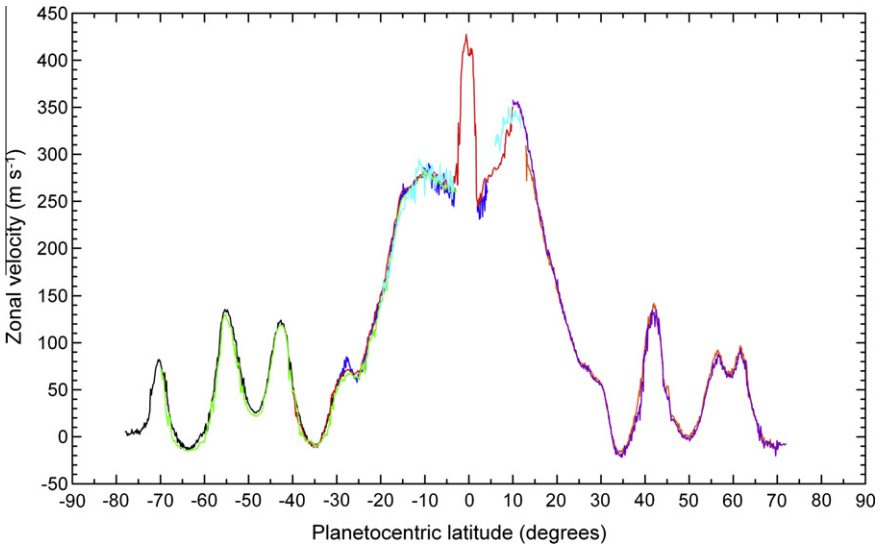

Fig. 2. Individual zonal wind profiles measured between September 2004 and January 2009 from Cassini ISS MT2 and MT3 images. 7 profiles are superimposed for the time periods listed in Table 1 where: black) COISS 2006 (MT2) covering the latitude interval from 78°S to 28°S; blue) COISS 2006 (MT1) from 30°S to 4°N; red) COISS 2009 from 40°S to 10°N; green) COISS 2012 from 70°S to 3°S; orange) COISS 2042 from 13 °N to 70°N; purple) COISS 2046 from 10°N to 72°N; cyan) COISS 2051 from 20°S to 4°S; cyan) COISS 2051 from 6°N to 12°N. (For interpretation of the references to color in this figure legend, the reader is referred to the web version of this article.)

Sánchez-Lavega (2001) to obtain global average profiles. We divided the complete profile into 0.2 latitude degree bins. In every bin we computed the average value of the latitude and velocity for the points inside. Velocity scatter was estimated according to expression (2). Uncertainties computed in this mode yielded average values between 5 m s^{-1} and 9 m s^{-1} for the respective CB and MT profiles which are consistent within the expected navigation errors, but which must also include scatter due to local dynamics (meteorology). These values should be sufficiently low to use these profiles to detect possible future wind changes. By following this procedure, distribution of latitude "centroid" points within every averaged bin was not exactly uniform and results were rounded off to 0.1 degrees. Within each bin, the average number of points was 42 in the CB filters and 33 in the MT case. The average CB and MT profiles are represented with their error bars in Fig. 3. The corresponding set of data for the average profiles can be retrieved as Tables 1 (CB data) and 2 (MT data) in the Supplementary Material section of the electronic version of this paper and is also available upon request to the author. Fig. 4 displays the estimated scatter for both profiles. In some latitude intervals for the CB profile, uncertainties are under 5 m s^{-1}. Scatter is larger at latitudes where there is a high meridional velocity gradient. At those regions small position shifts due to navigation errors produce large wind differences or a much larger scatter. Consequently, the largest scatter peaks are located at the strong velocity transitions in the narrow central equatorial jet and in the south polar region.

3.2. The (CB–MT) profile difference: vertical wind shears

Fig. 5 represents the (CB–MT) profile difference within its uncertainty envelope. Results are noteworthy for several reasons: (i) it is symmetrical around the equator while the individual MT profile is not; (ii) for absolute latitude values larger than 25°, the difference between both profiles is almost null; (iii) at the

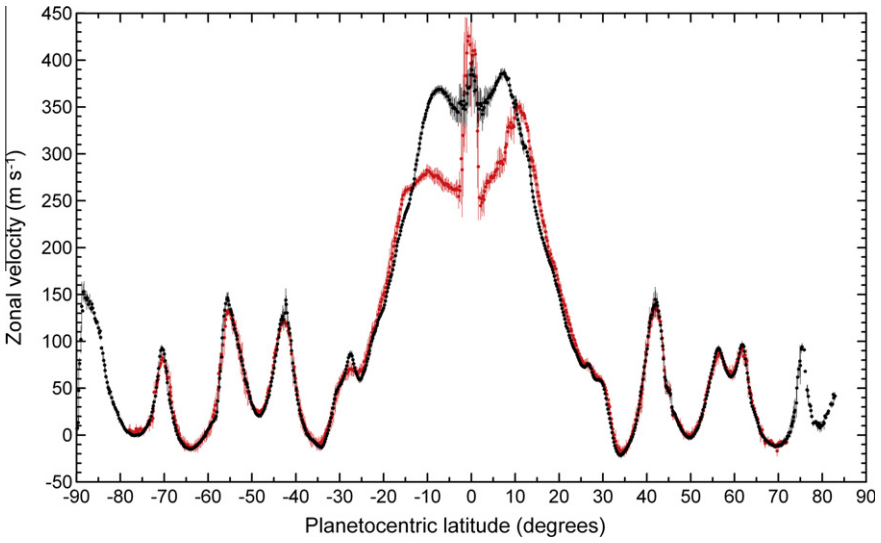

Fig. 3. Cassini average zonal wind profiles for the CB2 and CB3 (black), and the MT2 and MT3 (gray, red in the electronic version of this paper) filters. Complete individual data values are represented in Tables 1 and 2 as Supplementary Information along the electronic version of this paper. (For interpretation of the references to color in this figure legend, the reader is referred to the web version of this article.)

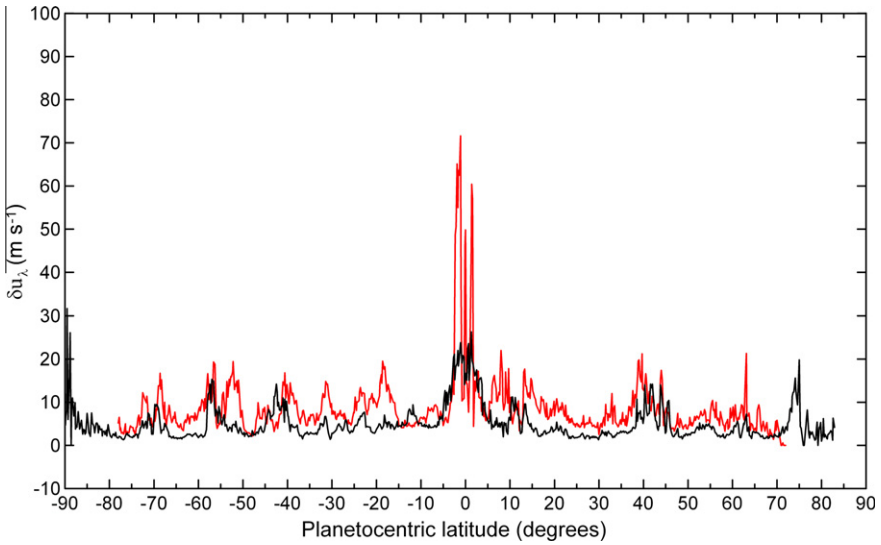

Fig. 4. Standard deviation for the Cassini CB2 and CB3 profile (black), and the MT2 and MT3 profile (gray, red in the electronic version of this paper). Values represent the standard deviation measured according to expression (2) in each individual 0.2 latitude-wide bin. (For interpretation of the references to color in this figure legend, the reader is referred to the web version of this article.)

equatorial region, there are two "inversion" wings where MT zonal winds are *stronger* than the CB counterparts, such velocity inversions span the approximate absolute planetocentric latitude interval from 10° to 25° and have an average intensity of ~ -30 m s^{-1}; (iv) except for the intense strong narrow jet (García-Melendo et al., 2010) which also presents a velocity inversion, the (CB–MT) difference at the equator is constant showing a plateau of $\sim +100$ m s^{-1}. Since the MT and CB profiles are measured at the same epoch and both sets of filters see different pressure levels, the conclusion is that Fig. 5 is displaying the effects of vertical wind shear. García-Melendo et al. (2009) showed that in the southern hemisphere a difference velocity of $\sim +20$ m s^{-1} is found at the centric latitudes of 27°S, 42°S, 55°S, and 70°S, which is due to the effect of wind shear between the ~250 mbar level observed in MT2 and MT3, and ~350 mbar observed in the CB filters. These wind results are consistent with vertical shears found by other authors from the thermal wind analysis (Conrath and Pirraglia, 1983; Fletcher et al., 2008). Fig. 5 reveals that this effect is also present at the northern hemisphere for the 40°N, 55°N and 62°N jet peaks, but with a lower intensity of $\sim +10$ m s^{-1}. In the equatorial region the shear is much stronger and is symmetric around the equator. In fact, the asymmetry in the MT profile in Figs. 2 and 3 exactly and simultaneously compensates the small asymmetric shape of the CB profile, indicating a constant vertical wind shear between the 60 mbar and the 500 mbar level in the interval $\sim|\varphi_c| < 7°$, and contributing to the symmetric location of the velocity minima inversion around the equator. By comparing the structure of the (CB–MT) difference with the thermal profiles of the upper troposphere retrieved by the CIRS instrument during the same 2004–2009 period presented by Fletcher et al. (2010), we can verify that the temperature maxima around the equator are at the same latitudes, 15°S and 12°N, where we observe the velocity inversion minima. These strong temperature peaks suggest, according to the thermal wind equation, that wind shear must be positive for the poleward side, and negative

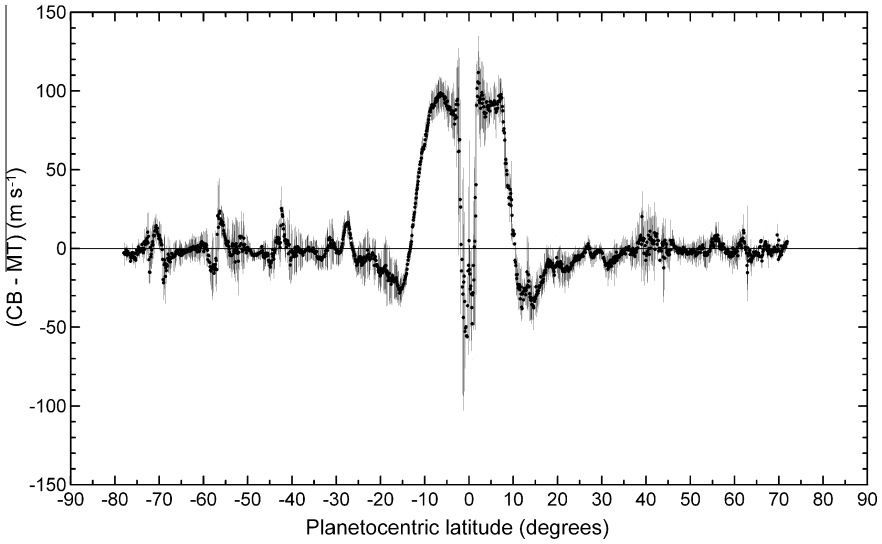

Fig. 5. (CB–MT) difference between the CB and MT average Cassini profiles represented in Fig. 3. Error bars are calculated assuming that estimated individual bin errors in the CB and MT profiles are independent.

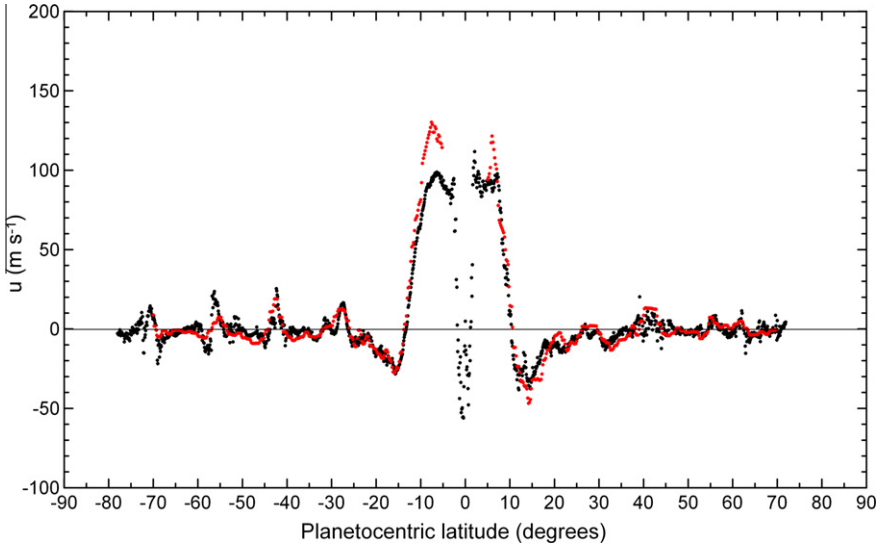

Fig. 6. Comparison between the (CB–MT) profile difference (solid dots) retrieved from Cassini ISS images and the vertical wind shear computed by using the thermal CIRS data reported by Fletcher et al. (2010) between 500 mbar and 100 mbar according to the thermal wind equation (gray dots, red in the electronic version of this paper). (For interpretation of the references to color in this figure legend, the reader is referred to the web version of this article.)

on the equatorward side. To directly estimate the effect of the thermal structure of the upper troposphere on the vertical wind shear, we integrated the thermal wind equation (Sánchez-Lavega, 2010).

$$\frac{\partial u}{\partial \ln p} = \frac{R}{f}\left(\frac{\partial T}{r\partial \varphi_c}\right)_p. \quad (3)$$

Here u is the zonal wind, p the pressure, $R = 3892\ \mathrm{J\,kg^{-1}\,K^{-1}}$ the specific gas constant, f the Coriolis parameter, T the temperature, and r the local planetary radius. We proceeded upwards from 500 mbar up to 100 mbar according to the estimated average thermal profiles obtained by Fletcher et al. (2010) in the interval $-70° \leqslant \varphi_c \leqslant 70°$, excluding the region $|\varphi_c| < 5°$ where the Coriolis parameter becomes too small. We used the average CB profile represented in Fig. 3, and assuming that it sits at ~500 mbar we integrated upwards the thermal wind equation. The resulting difference between the CB empirical profile and the integrated profile at 100 mbar (CB–Integrated), is compared with the measured (CB–MT) difference (Fig. 6). This calculation is an estimate which does not take into account possible variations of the pressure level of the cloud tops seen in the CB filters (from ~700 mbar to ~350 mbar) and the MT filters (from ~250 mbar to ~60 mbar). Nevertheless, the (CB–Integrated) profile difference is indeed able to capture all the essential structure of the (CB–MT) difference, including the small shear at the prograde jet peaks, the inversion wings at $|\varphi_c| \simeq 15°$, and the big equatorial velocity difference. This result shows complete consistency between the CIRS thermal data and the zonal wind field retrieved from ISS images. We can therefore conclude that most of the differences seen in the upper troposphere between the CB and MT profiles are coupled to the thermal structure through the thermal wind effect. CIRS data also indicate that vertical wind shear is not uniform. Shear is higher near the tropopause than at deeper levels. The lack of vertical wind shear at midlatitudes out of the prograde jet peaks, explains why the CB and MT zonal velocity measurements yield the same values. Zonal speed differences observed at the prograde jet peaks, inversion wings, and the equatorial region confirm that the MT and CB filters are truly sensing different altitudes and cloud tracers. García-Melendo et al. (2009, 2010), showed that cloud tracers seen in images obtained with CB and MT filters are different at the prograde jet peaks in the south hemisphere and equatorial region. Fig. 7 represents a cylindrical projection of two regions in the MT3 and CB3 filters (northern hemisphere, panels A and B respectively), and the MT2 and CB2 filters (southern hemisphere, panels C and D; for an equivalent version of the equator see Fig. 1 in García-Melendo et al., 2010). Although there are some common structures between the MT and CB images (large vortices, some of the wavy patterns, etc.), there is a wealth of small bright clouds (swirls, storms, etc.), only visible in the continuous band filters. There are also some common fine structures visible in both filters sets in latitudes with the same zonal winds. These images proof that we see different cloud tracers in the CB and MT images probing different altitudes. We then conclude that, the MT and CB profiles coincide because there is almost no vertical shear.

Not only is the vertical wind shear found at the southern midlatitudes consistent with the derived values from the thermal field presented by Fletcher et al. (2008), but also the smaller new values, ~10 m s^{-1} per scale height in the northern hemisphere jet peaks. The presence of vortices in regions very close to the equator ($\varphi_c < 10°$), with sizes L of the order of 10^5 m, see e.g. panels (a) and (b) of Fig. 1 in García-Melendo et al. (2010), indicates that probably even there the Rossby number is low enough for the thermal wind regime to be reasonable applied. In such a case the steep slopes of the thermal fields represented in Fig. 3 in Fletcher et al. (2010) for $|\varphi_c| \cong 10°$ would also account for part of the observed strong negative wind shear between the 500 mbar and 60 mbar.

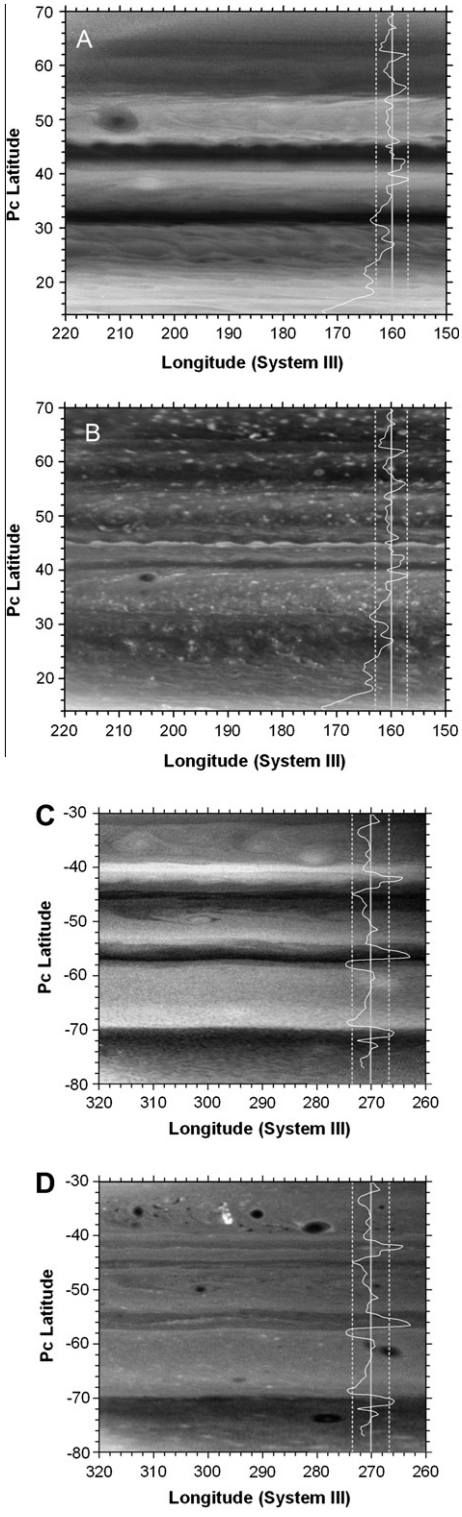

Fig. 7. Comparison of cloud morphologies in ISS images of the same area in the two sets of filters used in this work. Northern hemisphere: (A) MT3 filter and (B) CB3 filter. Southern hemisphere: (C) MT2 filter and (D) CB2 filter. The computed vertical shear from CIRS data between the 500 mbar and 100 mbar levels is overlapped on the right side of each panel. The vertical dashed lines represent the ±10 m s^{-1} limit (negative velocities are on the left of the vertical solid-line zero velocity reference). The small white cloud tracers visible in the CB filters mottling the images (small vortices, convective clouds, etc.) are not visible in the MT images. The same applies to many of the tracers present in the MT images. The difference is more dramatic for the northern hemisphere image pair.

4. Long-term variability of Saturn's wind profile

The available data sets that allow the study of the long-term variability of Saturn's winds can be divided in the following groups: (1) Before Voyagers, scarce historical observations (Sánchez_Lavega, 1982); (2) Voyager 1 and 2 encounters (1980–1981); (3) HST and ground-based imaging (1990–2004); (4) Cassini ISS (since 2004). The early observations of data set (3), years 1990–1997, correspond to a period of intense activity at the equator, following the Great White Spot event of 1990. We compare here the results from sets (2) and (3) with set (4).

4.1. The wind profile from 1994 to 2009

Before Cassini's spacecraft orbital insertion in 2004 and after the Voyager flybys, high resolution observations were not available until 1990, during and following the outbreak of a Great White Spot (GWS) (Sánchez-Lavega et al., 1991, 1993; Barnet et al., 1992; Beebe et al., 1992). However, the scarce historical data on motions spanning more than 100 years before 1990, indicates to first order that globally the winds remained stable (Sánchez_Lavega, 1982; Sánchez-Lavega et al., 1993). After 1990, the equator of Saturn kept being very active, showing a few more convective storms between 1994 and 1998 (Sánchez-Lavega et al., 1996, 1999). This cloud activity allowed to identify tracers and perform wind measurements until 2003 (Sánchez-Lavega et al., 2004). These HST wind measurements were obtained during the last northern hemisphere summer and autumn until the beginning of the winter between 2002 and 2004. After 1991, many of the wind measurements obtained from HST observations (Sánchez-Lavega et al., 2004) were in the strong methane absorbing 890 nm band which senses the high tropospheric haze, but they were combined with others obtained from images taken with broad band filters contributed by a thick atmospheric region. In the equatorial region all of them matched the methane 2004–2009 average Cassini profile as Fig. 8 shows, except for the strong narrow equatorial jet, which can only be detected with the high resolution of Cassini ISS images. Two points must be commented on Fig. 8. First, clouds seen at the equator in HST images between 1994 and 2003 were between the 50 mbar (1994 storm, Acarreta and Sánchez Lavega, 1999; Sánchez-Lavega et al., 1996), and 75 mbar levels (Sánchez-Lavega et al., 2003). These are the same levels probed by the Cassini MT2 and MT3 filters (Pérez-Hoyos and Sánchez-Lavega, 2006b; García-Melendo et al., 2010) Hazes at these levels are usually only detected by the methane absorbing band filters while continuum filters can see at deeper levels. However, radiative transfer analysis results showed (Pérez-Hoyos and Sánchez-Lavega, 2006b) that particle density injected by the convective clouds in the upper troposphere during the 1990 GWS event was so high that particle opacity dominated among all other opacity sources.

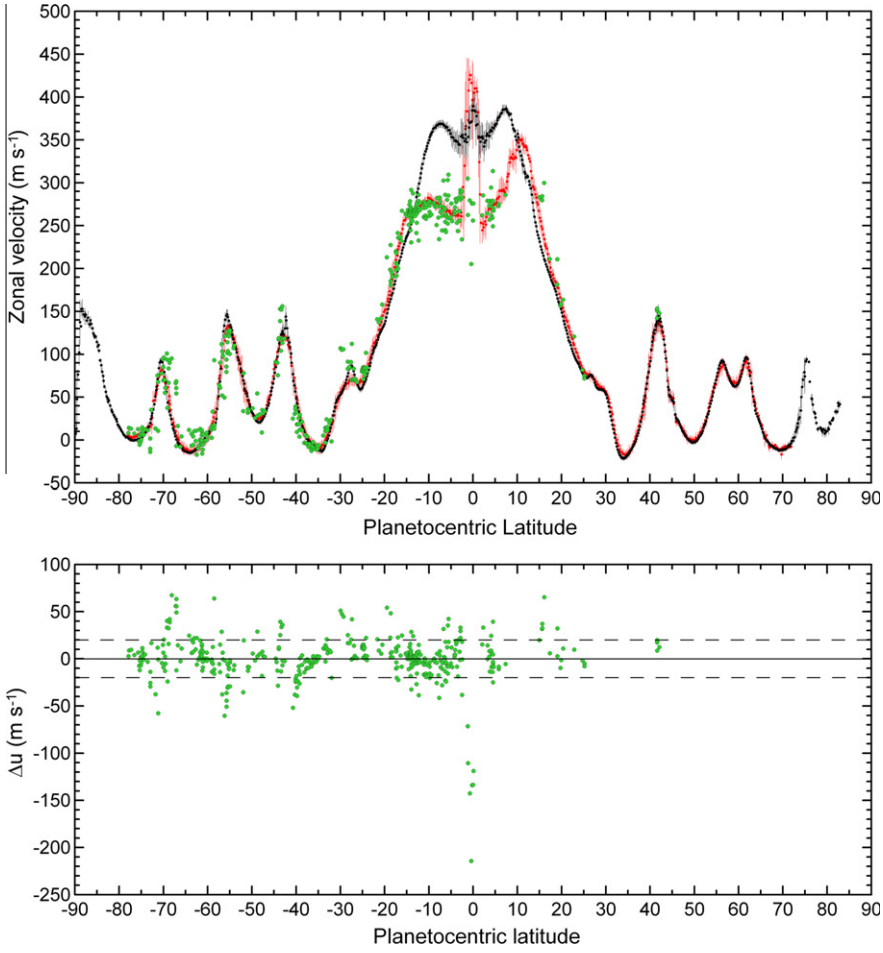

Fig. 8. Upper panel, superposition of the Cassini CB (black) and MT (gray, red in the electronic version) profiles to individual measurements performed on HST images (empty dots, green in the electronic version) from 1994 to 2003 (Sánchez-Lavega et al., 2004). Lower panel, differences between the individual HST observations and the Cassini MT profile. Average oscillations of the HST data are not larger than ~20 m s^{-1} (horizontal dashed lines), indicating that, within data scatter, the zonal velocity field sensed by the MT filter from 2004 to 2009 and the HST velocities observed from 1994 to 2003 are the same. (For interpretation of the references to color in this figure legend, the reader is referred to the web version of this article.)

Therefore, continuum filters (almost free from gas absorption and Rayleigh scattering) mostly saw the same cloud tops close to the tropopause than methane absorption filters, and wind measurements from continuum and methane filters were essentially the same, although part of the dispersion seen in the individual measurements in Fig. 8 may also be due to some vertical wind shear, as Sánchez-Lavega et al. (2004) pointed out. And second, the southern part of the methane profile at the equator retrieved at high resolution from Cassini images, remained stable from 1994 to 2009 after a half seasonal cycle through autumn and winter. Fletcher et al. (2010) showed that there have been some changes in the thermal structure of the planet's stratosphere and upper troposphere from 2004 to 2009, but during all this time results show that the equatorial zonal wind profile at the ~60 mbar level has remained unchanged. A preliminary analysis of Cassini data based on a few velocity measurements by Porco et al. (2005) suggested that HST data showed the effects of vertical shear. The wind profile presented therein shows a complete correspondence between the Cassini and HST data after 1994.

4.2. Comparison of the Voyager and Cassini profiles

Fig. 9 compares the CB and MT Cassini profiles with the Voyager profile (Sánchez-Lavega et al., 2000) mostly retrieved in the green and violet filters. The figure also includes the wind measurements during the equatorial GWS in 1990 (Barnet et al., 1992) that occurred between both spacecraft observations. Fig. 10 represents the profile differences between Voyager velocities and the CB and MT Cassini velocities, which are also compared with the (CB–MT) Cassini difference. Out of the equatorial region, for $|\varphi_c| > 30°$, all the profiles are fairly coincident. Some differences at the mid latitude jet peaks may be a combination of real changes

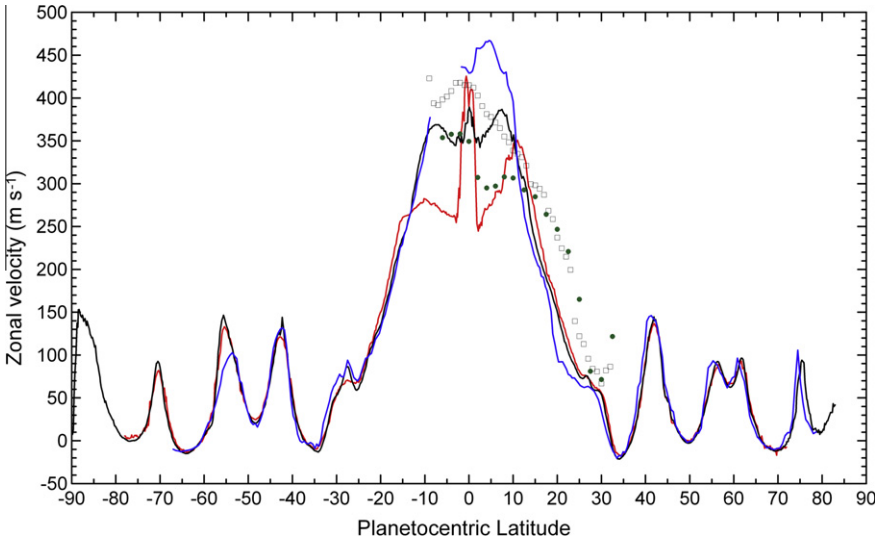

Fig. 9. Superposition of Cassini MT and CB profiles (thin lines, respectively red and black in the electronic version), and Sánchez-Lavega et al. (2000) thick solid line (blue in the electronic version), and HST profiles measured by Barnet et al. (1992) during the 1990 GWS with the F547N filter (squares) and the F889N filter (solid dots). (For interpretation of the references to color in this figure legend, the reader is referred to the web version of this article.)

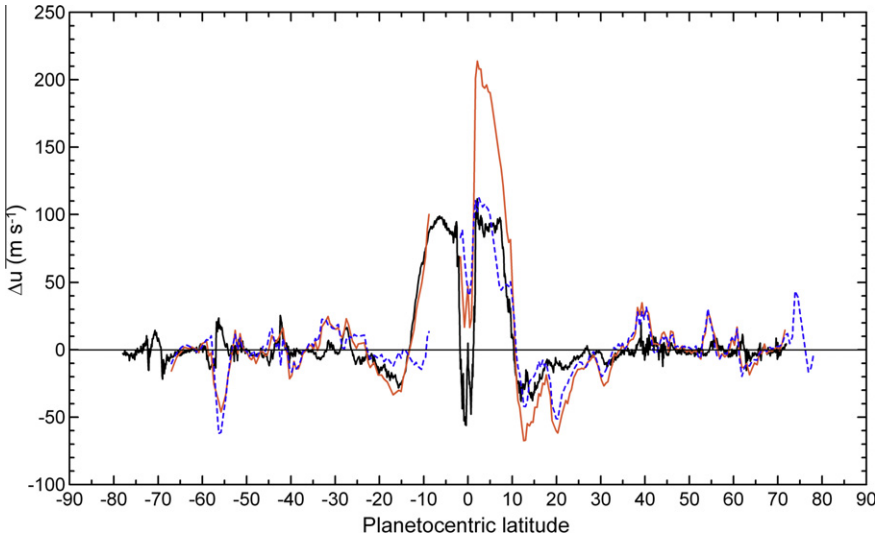

Fig. 10. Zonal wind profile differences between Cassini and Voyager wind measurements. The thick solid line represents the Cassini (CB–MT) profile difference, the thick gray (orange) and dotted (blue) lines the Voyager profile according to measurements by Sánchez-Lavega et al. (2000) minus the Cassini average MT and CB profiles respectively. (For interpretation of the references to color in this figure legend, the reader is referred to the web version of this article.)

and measurement uncertainties. From these figures we conclude that non-equatorial jets do not show at cloud level seasonal changes in their locations (for example seasonal meridional migrations), and if there are changes in their velocity, these are within 10% or less, and apparently not seasonal.

The most important differences between Voyager and Cassini profiles are found in the equatorial region. Differences amount to $\sim$100 m s^{-1} with the equatorial Cassini CB profile and $\sim$200 m s^{-1} with the MT profile. On the north side of the equatorial jet (the southern part is incomplete in Voyager data due to the blocking effect of the rings), there is also a large velocity inversion between 10°N and 30°N when compared with the Cassini winds, reaching $\sim$60 m s^{-1}. According to the results presented by Pérez-Hoyos and Sánchez-Lavega (2006b), the differences related to the equatorial region can only be reasonably explained if there has been a real slow down of the wind speed, although it may also be combined with vertical wind shear effects (see Section 5) Perhaps this slow down was induced by the 1990 GWS, although it is unclear according to numerical modeling, which predicted a small influence of the disturbance (Sayanagi and Showman, 2007).

5. Discussion

Our analysis of CIRS data indicates there is a real difference between the northern and southern vertical wind shears at the mid-latitude jet peaks. The measured difference is not linked to the detection of tropospheric hazes at different altitudes by the MT and CB filters, but to the different northern and southern thermal fields. Thermal wind integration shows a $\sim$20 m s^{-1} amplitude in the southern hemisphere and $\sim$10 m s^{-1} in the northern one between 500 mbar and 100 mbar, fully consistent with our observations. Muñoz et al. (2004) found that during Saturn's northern hemisphere autumn, tropospheric hazes are lower in the southern hemisphere than in the northern one, perhaps due to a seasonal effect. But seasonal changes do not show a clear impact on the thermal field for $p > 100$ mbar (Fletcher et al., 2010) able to explain vertical wind shear differences between both hemispheres at mid-latitudes. It is evident that much longer high resolution data series (zonal velocity and thermal field) are needed. In a more global view, Stam et al. (2001), Muñoz et al. (2004), Pérez-Hoyos et al. (2005) and Karkoschka and Tomasko (2005) found that hazes are denser at the equator. This global picture of high tropospheric hazes sinking to higher pressure levels is also fully consistent with an 890 nm view of the planet in the MT3 filter. Fig. 11 is a meridional, Lambert corrected, photometric scan of Saturn, which shows how the geometric albedo rapidly decreases out of the equatorial region, indicating that the pressure level of the visible high tropospheric haze rapidly increases at mid-latitudes.

An interesting finding is the velocity inversion in the $10° < |\varphi_c| < 25°$ intervals. It is consistent with all the previously reported results derived from Voyager (Conrath and Pirraglia, 1983), and Cassini (Fletcher et al., 2008) thermal results. In particular, the presence of the two velocity inversion wings exactly matches the latitude intervals where Conrath and Pirraglia (1983) predicted strong positive vertical wind shear at the 150 mbar level derived from Voyager infrared thermal measurements. This is confirmed by integration of the thermal wind equation almost exactly matching the (CB–MT) profile difference. This is a subtle structure of the upper tropopause which appears to be stable at least during the whole last saturnian year from Voyager to Cassini. Results also show that strong positive shears with $\partial u/\partial z \simeq 40$ m s^{-1} H^{-1} at the equatorial jet are related to the thermal structure of Saturn's upper troposphere.

Measurements of the full wind profile in time give us a detailed view of the long term changes in Saturn's cloud top global circulation. We may distinguish two different periods marked by the 1990 GWS event. After 1990, all HST and ground-based measurements (Sánchez-Lavega et al., 2004) indicate that, aside the narrow equatorial jet whose time evolution is still unknown, winds have remained unchanged within the measurement uncertainties. Fletcher et al. (2010) found that temperature variations from 2004 to 2009, within measurement errors, were small at the upper troposphere except perhaps at the 200 mbar level, although such variability was uncertain. Such temperature stability during the measurement period explains why the MT profile has remained also stable. Until 1990 we have only two sets of profiles, one derived from Voyager observations (Smith et al., 1982; Ingersoll et al., 1984; Sánchez-Lavega et al., 2000; etc.), and another one retrieved during the 1990 storm (Barnet et al., 1992). The 1990

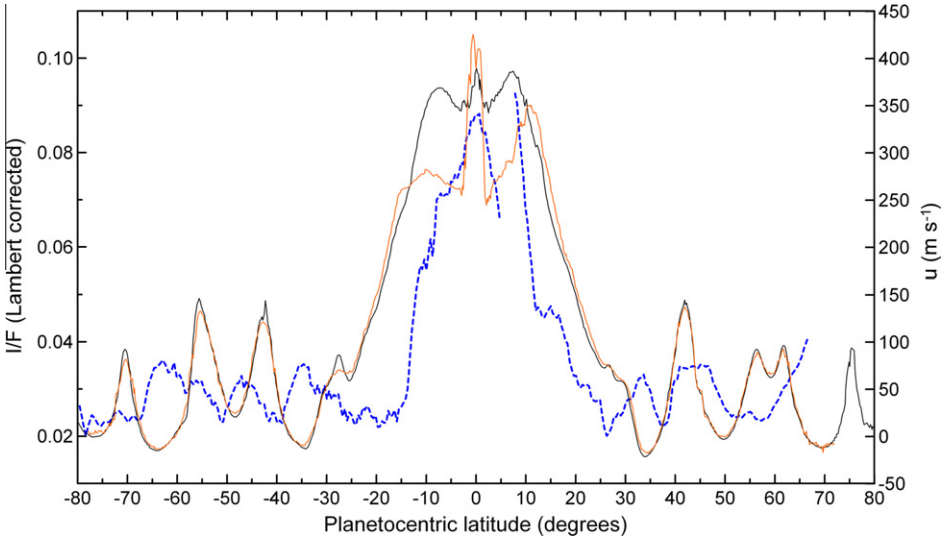

Fig. 11. Geometric albedo of Saturn (thick dashed line) in the MT3 filter for images N1459996514 (April 2004, $\alpha = 66°$, southern hemisphere and equator), and W1611017605 (January 2009, $\alpha = 27°$, northern hemisphere). The rapidly decreasing albedo towards higher latitudes is consistent with the detection of higher and optically thicker hazes at the equator. In the background (thin line) are represented the Cassini CB (thin solid) and MT (thin gray, orange) zonal winds. (For interpretation of the references to color in this figure legend, the reader is referred to the web version of this article.)

profile retrieved in the F889N HST filter shows velocities as high as the Cassini CB profile, and F547N measurements are close to the Voyager profile and higher than Cassini results. As indicated by Sánchez-Lavega et al. (2004), the 1990 storm injected aerosols changing the pressure detection level by the methane absorbing band filters from ~300 mbar to ~50 mbar. But still, this cannot explain the differences between the Voyager and Cassini profiles. According to the radiative transfer analysis performed by Pérez-Hoyos and Sánchez-Lavega (2006b) (see Fig. 12 in their paper), Voyager green filter probed a level similar to that seen by the continuum Cassini CB filters, therefore a difference up to 100 m s^{-1} between Voyager and Cassini profiles is still unexplained. The Voyager measurements should be located at 2–3 bar in order to agree with the HST and Cassini post-GWS scenario assuming that the ~40 m s^{-1} H^{-1} vertical shear remains constant down to these levels, which may be unlikely in view of the thermal fields retrieved by Cassini CIRS. This possibility seems to be precluded by the analysis performed by Pérez-Hoyos and Sánchez-Lavega (2006b), in particular due to the observation of fast structures in the violet filter. Nevertheless there is still a chance that these fast tracers were deeply rooted and able to survive the vertical wind shear during their life times, being therefore representative of the flow speeds deeper in the atmosphere and not at the level of their cloud tops.

At the near infrared band of 5 μm, Cassini's Visual and Infrared Mapping Spectrometer (VIMS) is able to observe the planet at levels down to 5 bar (Bjoraker et al., 2007), although cloud features probably do not allow to see deeper than 2 bar (Baines et al., 2005; Momary et al., 2006). Choi et al. (2009) measured an almost complete Saturn's zonal wind profile in the 5 μm band. VIMS retrieved wind speeds at the equatorial region are similar to those observed by Voyager. However Choi et al. estimated that to account for the 100 m s^{-1} difference between the 700 mbar and the 2 bar levels (about 1 scale height) a meridional temperature gradient of ~1 K per 1000 km would be needed, which is about 10 times larger than the observed temperature gradient at 500 mbar at the equatorial region and the same order of magnitude as the temperature gradients at 100 mbar. This is difficult to reconcile with a progressively smoother thermal field for deeper levels. Out of the equatorial region ($|\varphi_c| > 10°$), geostrophic balance and thermal wind must prevail in the steady state. In this situation, horizontal thermal gradients along horizontal isobaric surfaces must be steep enough to ensure vertical shear. Voyager and Cassini thermal field results (Conrath and Pirraglia, 1983; Fletcher et al., 2010) indicate that vertical wind shear is not uniform and that temperature gradients smooth out at deeper regions where vertical shear diminishes vanishing at the adiabatic region. The situation gets even more puzzling to explain a 100 m s^{-1} speed increase detected in the VIMS data at the 45°S jet peak at ~2 bar. The ~5 K per 1000 km estimate by Choi et al. is far larger than any temperature gradient measured at that latitude by CIRS between 100 mbar and 500 mbar. But we must be careful in a direct comparison between the retrieved VIMS and ISS winds, the apparent discrepancies soften if the features tracked at 5 μm lie deeper than the 2 bar level. Moreover, we have no direct thermal data at the 2 bar level, and invoking only the thermal wind at deeper levels below the visible cloud deck could overlook other processes at the jet peaks.

Saturn undergoes strong seasonal insolation variations, a cycle combined with the ring's shadow effect (Pérez-Hoyos and Sánchez-Lavega, 2006a). As determined from Cassini data and comparisons with Voyager data, Saturn's emitted power presents both locally seasonal and global interannual variability (Li et al., 2010). These changes seem not to be reflected in changes in the nearly constant zonal winds except at the equator where the 1990 GWS storm injected huge amounts of aerosols in the upper troposphere which changed the opacity of the hazes altering the radiative energy transfer equilibrium and thermal field. Therefore, there is the possibility of a real large-scale dynamic change from the 1990 GWS which combines cloud top level changes, vertical shear changes, and perhaps changes at deeper levels due to the vertical transport of mass and angular momentum (Hueso and Sánchez-Lavega, 2004). The analysis of the recent GWS that erupted at North Tropical latitudes on December 5th 2010 (Fletcher et al., 2011; Sánchez-Lavega et al., 2011) indicates no major changes in the wind profile at the upper cloud level during the first 2 months of evolution of the phenomena. A more in deep analysis of Cassini ISS images (Fischer et al., 2011) will help to solve this point.

6. Summary

In this paper we have presented the full zonal wind profiles of Saturn averaged in time (2004–2009) and longitude from data obtained with the Cassini ISS instrument using CB and MT filter sets. These profiles allow precise comparisons with previous wind measurements, obtained since 1980 and extend the coverage of the wind profile datasets through a full Saturn year. The most important features are: (1) Outside the equatorial jet that spans from 35°N to 35°S, the jet wind structure remained essentially unchanged in intensity and jet location during a whole Saturn year (within error uncertainties). Apparently the seasonal insolation cycle does not affect the global wind structure at cloud level. (2) Velocity differences between the CB and MT profiles are fully consistent with the Cassini CIRS thermal data (Fletcher et al., 2010) via the thermal vertical wind shear effect. (3) The equatorial jet is also a permanent feature of Saturn's global circulation but shows high temporal variability. Cassini ISS images in CB and MT from 2004 to 2009 confirm the strong vertical wind shear previously detected in HST images both during the GWS event in 1990 and from 1994 to 2003. During 2004–2009 we measured a ~100 m s^{-1} wind speed difference between the MT and CB profiles that radiative transfer modeling and an estimation of the thermal wind effect proof to be due to vertical wind shear. (4) The presence of an intense narrow jet (from 3°N and 3°S) at the equator, specially visible in the MT2 and MT3 filters (discussed in García-Melendo et al. (2010)) is a conspicuous feature of the equatorial super-rotation at least during years 2004–2009. (5) In this Cassini period we also detected two +30 m s^{-1} velocity inversion wings between $10° < |\varphi_c| < 25°$ which has also been a persistent feature during the last 30 years. At present we do not know how the seasonal insolation cycle at the equator (including ring shadowing) may affect the results (4) and (5). (6) The major temporal difference in the equatorial jet occurred when comparing the Voyager (1980–1981) with the HST and ground-based periods (1990–2003) and Cassini (2004–2009). The conspicuous differences we see between the profiles derived in these periods are probably due to real major changes in the equatorial circulation, although it is still unclear if they were introduced by the outburst of the GWS event in 1990, which perhaps affected the dynamics and cloud structure of the equatorial region. Vertical wind shear may also contribute to the observed difference, but cloud tracers seen by Voyager cloud tops were not much deeper than those seen in the Cassini continuum bands (Pérez-Hoyos and Sánchez-Lavega, 2006b). Therefore the ~100 m s^{-1} difference between Voyager and Cassini cannot be accounted for by only invoking vertical wind shear. Separation of the three effects (vertical wind shear, GWS induced wind variability and cloud structure, and seasonal insolation changes) during the whole Saturn year in the equatorial area is not an easy issue with the data in hand. We need continuous observations to see, for example, whether the equatorial winds follow the seasonal insolation cycle when no large scale storms are present. The high resolution (CB–MT) profile difference reveals itself as a powerful

monitoring tool for the upcoming Cassini observations during the next years while the saturnian northern summer solstice approaches and insolation conditions change, which should be combined with the analysis of the thermal field to obtain a good understanding of the equatorial dynamics. High resolution Cassini observations and wind monitoring during the Solstice Mission following Saturn's changing season and the new 2010 GWS may be crucial to understand Saturn's super rotation conundrum.

Acknowledgments

We thank Leigh Fletcher for sharing with us the CIRS thermal data used in our thermal wind computations. We are also grateful to Sabela de la Torre from the Universitat Politècnica de Catalunya, whose image correlation software was used to perform some of the velocity measurements. This work has been funded by Spanish MEC AYA2009-10701 with FEDER support and Grupos Gobierno Vasco IT-464-07.

Appendix A. Supplementary material

Supplementary data associated with this article can be found, in the online version, at doi:10.1016/j.icarus.2011.07.005.

References

Acarreta, J.R., Sánchez Lavega, A., 1999. Vertical cloud structure in Saturn's 1990 equatorial storm. Icarus 137, 24–33.
Acton, Ch.H., 1995. Ancillary data services of NASA's Navigation and Ancillary Information Facility. Planet. Space Sci. 44, 65–70.
Baines, K.H., Momary, T.W., Roos-Serote, M., 2005. The deep winds of Saturn: First measurements of the zonal wind field near the two-bar level. Bull. Am. Astron. Soc. 37, 658.
Baines, K.H. et al., 2009. Saturn's north polar cyclone and hexagon at depth revealed by Cassini/VIMS. Plan Space Sci. 57, 1671–1681. doi:10.1016/j.pss.2009.06.026.
Barnet, C.D., 1990. Saturn's Seasonal Winds and Temperature: The Effect of the Ring System on the Troposphere and Stratosphere. Thesis, New Mexico State University.
Barnet, C.D., Westphal, J.A., Beebe, R.F., Huber, L.F., 1992. Hubble Space Telescope observations of the 1990 equatorial disturbance on Saturn: Zonal winds and central meridian albedos. Icarus 100, 499–511.
Beebe, R.F., Barnet, C., Sada, P.V., Murrell, A.S., 1992. The onset and growth of the 1990 equatorial disturbance on Saturn. Icarus 95, 163–172.
Bjoraker, G.L., Chanover, N.J., Glenar, D.A., Hewagama, T., 2007. Saturn's deep cloud structure derived from 5-micron spectra, Eos (Fall Suppl.) 88(52). Abstract P31A-0184.
Choi, D.S., Showman, A.P., Brown, R., 2009. Cloud features and zonal wind measurements of Saturn's atmosphere as observed by Cassini/VIMS. J. Geophys. Res. 114, E04007.
Conrath, B.J., Pirraglia, J.A., 1983. Thermal structure of Saturn from Voyager infrared measurements – Implications for atmospheric dynamics. Icarus 53, 286–292.
Del Genio, A.D. et al., 2007. Saturn eddy momentum fluxes and convection: First estimates from Cassini images. Icarus 189, 479–492.
Del Genio, A.D. et al., 2009. Saturn atmospheric structure and dynamics. In: Dougherty, M.K., Esposito, L.W., Krimigis, S.M. (Eds.), Saturn from Cassini–Huygens. Springer-Verlag, pp. 113–159.
Desch, M.D., Kaiser, M.L., 1981. Voyager measurements of the rotation period of Saturn's magnetic field. Geophys. Res. Lett. 8, 253–256.
Dyudina, U.A. et al., 2008. Dynamics of Saturn's south polar vortex. Science 319, 1801. doi:10.1126/science.1153633.
Fischer, G. et al., 2011. Seasonal variation of giant thunderstorms on Saturn. Nature 475, 75–78.
Fletcher, L.N. et al., 2008. Temperature and composition of Saturn's polar hot spots and hexagon. Science 319, 79–81.
Fletcher, L.N. et al., 2010. Seasonal change on Saturn from Cassini/CIRS observations, 2004–2009. Icarus 208, 337–352.
Fletcher, L.N. et al., 2011. Thermal structure and dynamics of Saturn's northern springtime disturbance. Science 332, 1413–1417.
García-Melendo, E., Sánchez-Lavega, A., 2001. A study of the stability of jovian zonal winds from HST images: 1995–2000. Icarus 152, 316–330.
García-Melendo, E., Sánchez-Lavega, A., Rojas, J.F., Pérez-Hoyos, S., Hueso, R., 2009. Vertical shears in Saturn's eastward jets at cloud level. Icarus 201, 818–820. doi:10.1016/j.icarus.2009.02.022.
García-Melendo, E., Sánchez-Lavega, A., Legarreta, J., Pérez-Hoyos, S., Hueso, R., 2010. A strong high altitude narrow jet detected at Saturn's equator. Geophys. Res. Lett. 37, L22204. doi:10.1029/2010GL045434.
Godfrey, D.A., 1988. A hexagonal feature around Saturn's north pole. Icarus 76, 335–356.
Heimpel, M., Aurnou, J., 2007. Turbulent convection on rapidly rotation spherical shells: A model for equatorial and high latitude jets on Jupiter and Saturn. Icarus 187, 540–557.
Hueso, R., Sánchez-Lavega, A., 2004. A three-dimensional model of moist convection for the giant planets II: Saturn's water and ammonia moist convective storms. Icarus 2004, 368–378.
Hueso, R. et al., 2010. The Planetary Laboratory for Image Analysis (PLIA). Adv. Space Res. 46, 1120–1138.
Ingersoll, A.P., Beebe, R.F., Conrath, B.J., Hunt, G.E., 1984. Structure and dynamics of Saturn's atmosphere. In: Gehrels, T., Matthews, M.S. (Eds.), Saturn. Univ. of Arizona Press, Tucson, pp. 195–238.
Ingersoll, A.P. et al., 2004. Dynamics of Jupiter's atmosphere. In: Bagenal, F., McKinnon, W., Dowling, T. (Eds.), Jupiter: The Planet, Satellites & Magnetosphere. Cambridge University Press, Cambridge, pp. 105–128.
Jones, A.C., Kuzanyan, K.M., 2009. Compressible convection in the deep atmospheres of giant planets. Icarus 204, 227–238.
Karkoschka, E., Tomasko, M.G., 1992. Saturn's upper troposphere 1986–1989. Icarus 97, 161–181.
Karkoschka, E., Tomasko, M.G., 2005. Saturn's vertical and latitudinal cloud structure 1991–2004 from HST imaging in 30 filters. Icarus 179, 195–221.
Kaspi, Y., Flierl, G.R., Showman, A.P., 2009. The deep wind structure of the giant planets: Results from an anelastic general circulation model. Icarus 202, 525–542.
Li, L. et al., 2010. Saturn's emitted power. J. Geophys. Res. 115, E11002.
Momary, T.W., Baines, K.H., The Cassini/VIMS Science Team, 2006. The zoology of Saturn: The bizarre features unveiled by the 5 micron eyes of Cassini/VIMS. Bull. Am. Astron. Soc. 38, 499.
Muñoz, O., Moreno, F., Molina, A., Grodent, D., Gérard, J.C., Dols, V., 2004. Study of the vertical structure of Saturn's atmosphere using HST/WFPC2 images. Icarus 169, 413–428.
Ortiz, J.L., Moreno, F., Molina, A., 1996. Saturn 1991–1996: Clouds and hazes. Icarus 119, 53–66.
Pérez_Hoyos, S., Sánchez_Lavega, A., 2006a. Solar flux in Saturn's atmosphere: Penetration and heating rates in the aerosol and cloud layers. Icarus 180, 368–378.
Pérez-Hoyos, S., Sánchez-Lavega, A., 2006b. On the vertical wind shear of Saturn's equatorial jet at cloud level. Icarus 180, 161–175.
Pérez-Hoyos, S., Sánchez-Lavega, A., Frech, R.G., Rojas, J.F., 2005. Saturn's cloud structure and temporal evolution from ten years of Hubble Space Telescope images (1994–2003). Icarus 176, 155–174.
Porco, C.C. et al., 2004. Cassini Imaging Science: Instrument characteristics and anticipated scientific investigations at Saturn. Space Sci. Rev. 115, 363–497.
Porco, C.C. et al., 2005. Cassini Imaging Science: Initial results on Saturn's atmosphere. Science 307, 1243–1247.
Read, P.L. et al., 2007. Dynamics of convectively driven banded jets in the laboratory. J. Atmos. Sci. 64, 4031–4052. doi:10.1175/2007JAS2219.1.
Read, P.L., Dowling, T.E., Schubert, G., 2009. Saturn's rotation period from its atmospheric planetary-wave configuration. Nature 460, 608–610.
Sánchez Lavega, A., 1982. Motions in Saturn's atmosphere: Observations before Voyager encounters. Icarus 49, 1–16.
Sánchez-Lavega, A., 2005. How long is the day on Saturn? Science 307, 1223–1224.
Sánchez-Lavega, A., 2010. An Introduction to Planetary Atmospheres. Taylor & Francis, CRC Press, Boca Raton, Florida, 587pp..
Sánchez-Lavega, A., Colas, F., Lecacheux, J., Laques, P., Miyazaki, I., Parker, D., 1991. The Great White Spot and disturbances in Saturn's equatorial atmosphere during 1990. Nature 353, 397–401.
Sánchez-Lavega, A., Lecacheux, J., Colas, F., Laques, P., 1993. Temporal behavior of cloud morphologies and motions in Saturn's atmosphere. J. Geophys. Res. 98, 18857–18872.
Sánchez-Lavega, A. et al., 1996. Large-scale storms in Saturn's atmosphere during 1994. Science 271, 631–634.
Sánchez-Lavega, A., Lecacheux, J., Colas, F., Rojas, J.F., Gómez, J.M., 1999. Discrete cloud activity in Saturn's equator during 1995, 1996 and 1997. Planet. Space. Sci. 47, 1277–1283.
Sánchez-Lavega, A., Rojas, J.F., Sada, P.V., 2000. Saturn's zonal winds at cloud level. Icarus 147, 405–420.
Sánchez-Lavega, A., Pérez-Hoyos, S., Rojas, J.F., Hueso, R., French, R.G., 2003. A strong decrease in Saturn's equatorial jet at cloud level. Nature 423, 623–625.
Sánchez-Lavega, A., Hueso, R., Pérez-Hoyos, S., Rojas, J.F., French, R.G., 2004. Saturn's cloud morphology and zonal winds before the Cassini encounter. Icarus 170, 519–523.
Sánchez-Lavega, A., Hueso, R., Pérez-Hoyos, S., Rojas, J.F., 2006. A strong vortex in Saturn's south pole. Icarus 184, 524–531. doi:10.1016/j.icarus.2006.05.020.
Sánchez-Lavega, A., Hueso, R., Pérez-Hoyos, S., 2007. The three-dimensional structure of Saturn's equatorial jet at cloud level. Icarus 187, 510–519.
Sánchez-Lavega, A. et al., 2011. Deep winds beneath Saturn's upper clouds from a seasonal long-lived planetary-scale storm. Nature 475, 71–75. doi:10.1038/nature10203.
Sayanagi, K.M., Showman, A.P., 2007. Effects of a large convective storm on Saturn's equatorial jet. Icarus 187, 520–539.
Seidelmann, P.K. et al., 2007. Report of the IAU/IAG working group on cartographic coordinates and rotational elements: 2006. Celestial Mech. Dyn. Astron. 98, 155–180.
Showman, A.P., 2009. Windy clues to Saturn's spin. Nature 460, 582–583.
Simon-Miller, A.A., 1999. The structure and temporal stability of Jupiter's zonal winds: A study of the North Tropical Region. Icarus 141, 29–39.
Smith, B.A. et al., 1982. A new look at the Saturn system: The Voyager 2 images. Science 215, 504–537.

Stam, D.M., Banfield, D., Gierasch, P., Nicholson, P.D., Matthews, K., 2001. Near-IR Spectrophotometry of Saturnian Aerosols-Meridional and vertical distribution. Icarus 152, 407–422.

Tomasko, M.G., West, R.A., Orton, G.S., Teifel, V.G., 1984. Clouds and aerosols in Saturn's atmosphere. In: Gehrels, T., Matthews, M.S. (Eds.), Saturn. Univ. of Arizona Press, Tucson, pp. 150–194.

Vasavada, A.R. et al., 2006. Cassini imaging of Saturn: Southern hemisphere winds and vortices. J. Geophys. Res. 111, E05004.

West, R.A., Baines, K.H., Karkoschka, E., Sánchez-Lavega, A., 2009. Clouds and aerosols in Saturn's atmosphere. In: Dougherty, M.K., Esposito, L.W., Krimigis, S.M. (Eds.), Saturn from Cassini–Huygens. Springer, New York, pp. 113–159.